



Science Arts & Métiers (SAM)

is an open access repository that collects the work of Arts et Métiers Institute of Technology researchers and makes it freely available over the web where possible.

This is an author-deposited version published in: <https://sam.ensam.eu>
Handle ID: <http://hdl.handle.net/10985/21276>

To cite this version :





Mathieu FRANÇOIS, Sangil HAN, Corinne DUPUY, Simon TURPAULT, Mehdi MIMOUNA, Ferdinando SALVATORE, Joël RECH, Patrice PEYRE, Mickaël RIVETTE, Frederic SEGONDS - Electromagnetic performance of Ti6Al4V and AISi7Mg0.6 waveguides with laser beam melting (LBM) produced and abrasive flow machining (AFM) finished internal surfaces - Journal of Electromagnetic Waves and Applications - Vol. 35, n°18, p.2510-2526 - 2021

Any correspondence concerning this service should be sent to the repository

Administrator : scienceouverte@ensam.eu



Electromagnetic performance of Ti6Al4V and AlSi7Mg0.6 waveguides with laser beam melting (LBM) produced and abrasive flow machining (AFM) finished internal surfaces

Mathieu François ^{a,b,d,e}, Sangil Han^c, Frédéric Segonds ^d, Corinne Dupuy^a, Mickaël Rivette ^e, Simon Turpault^f, Mehdi Mimouna^b, Ferdinando Salvatore^c, Joël Rech^c and Patrice Peyre ^a

^aProcesses and Engineering in Mechanics and Materials Laboratory (PIMM), UMR CNRS 8006/Arts et Métiers Institute of Technology/CNAM, Paris, France; ^bOPS-Hardware Techno. Tools & Engineering, Thales SIX GTS France, Gennevilliers, France; ^cUniversité de Lyon, Ecole Centrale de Lyon – ENISE, LTDS, UMR CNRS 5513, Saint-Étienne, France; ^dProduct Design and Innovation Laboratory (LCPI), Arts et Métiers Institute of Technology, Paris, France; ^eManufacturing Engineering and Control Laboratory (LCFC), Arts et Métiers Institute of Technology, Metz, France; ^fPS-Hardware Techno. Tools & Engineering, Thales SIX GTS France, Cholet, France

ABSTRACT

Metal additive manufacturing processes, such as laser beam melting (LBM), can play a key role in developing antenna-feed chains because monolithic and multifunctional parts can be manufactured with high geometric freedom in the design phase. Using LBM technology, lighter and more compact antennas can be produced and manufacturing costs can be reduced. However, the surface roughness of internal surfaces in waveguides produced by LBM is much higher (about $10\text{ }\mu\text{m } Ra$) than that produced by conventional manufacturing technologies. Consequently, such high surface roughness of the internal surface can affect electrical current propagation through the waveguide and corresponding transmitted power. In this paper, abrasive flow machining (AFM) was used to reduce the surface roughness of the internal surfaces of four different waveguides used at both K and Q bands. A significant reduction in the transmission loss at both K and Q bands was observed as their internal surface roughness decreased from about $10\text{ }\mu\text{m}$ to $1\text{ }\mu\text{m } Ra$. This was assumed to be due to an increase of the internal surface electrical conductivity with the decrease of roughness in waveguides channels.

1. Introduction

There has been great technological advances in satellite communications (SatCom) antenna over the past years. However, waveguides, which are installed in the SatCom antenna, have been made by conventional manufacturing processes, such as CNC-machining and electrical discharge machining (EDM). With such conventional

manufacturing processes, a great amount of materials should be removed to produce their internal channels, increasing their manufacturing time and costs. Moreover, the degree of freedom in waveguide design was restricted by manufacturing processes.

With the emergence of additive manufacturing (AM) processes, and especially laser beam melting (LBM), more flexible waveguide designs became possible, lighter and more compact. Additionally, their manufacturing time and cost are reduced significantly.

A number of studies [1–9] have been dedicated to assess the electromagnetic performances of passive microwave waveguide components produced by AM. The transmission performance of rectangular waveguides, which have been manufactured by conventional manufacturing processes, were investigated. Aluminum (AlSi7Mg0.6) and titanium (Ti6Al4V) rectangular waveguides were fabricated with additive manufacturing. Their transmission losses were found to be two times higher than simulated values at X-band (8–12 GHz) and Ka-band (27–40 GHz) [1,2]. For a copper (CuSn15) rectangular waveguide fabricated with AM, its transmission loss at the V-band (40–75 GHz) was four times bigger than that produced by machining [3]. Similar transmission losses at X-band (8–12 GHz) and E-band (60–90 GHz) were also observed in more complex waveguide shapes fabricated by AM [1,2].

It was noted that transmission losses in AM-built waveguides were greater than theoretical values regardless of the shape of waveguides or the frequency band. Thus, it was acknowledged that surface roughness of the internal surface in waveguides affected its transmission loss. Tchhoffolo-Talom and Turpault [2] performed chemical treatments (Surtec 650) on the internal surfaces of waveguides and indicated that transmission losses at the X-band and the Ka-band were reduced as compared to those without chemical treatments. Zhang et al. [3] showed that the transmission loss increases with increases of the internal surface roughness. Lorente et al. [5] polished surfaces of microwave filters manufactured by laser beam melting (LBM) and found that its Q efficiency increased by about 70% as compared to that without polishing. More precisely, Wang and Cui [8] and Braunsch et al. [9] indicated that rough internal channels surfaces led to a decrease in the electrical conductivity, causing severe transmission loss.

High surface roughness (about $10\text{ }\mu\text{m Ra}$) in the LBM internal channel results from layer-by-layer manufacturing in additive manufacturing. Surface roughness, in particular, on inclined or curved surfaces is influenced by ‘staircase effect’ [10–12], which is illustrated in Figure 1.

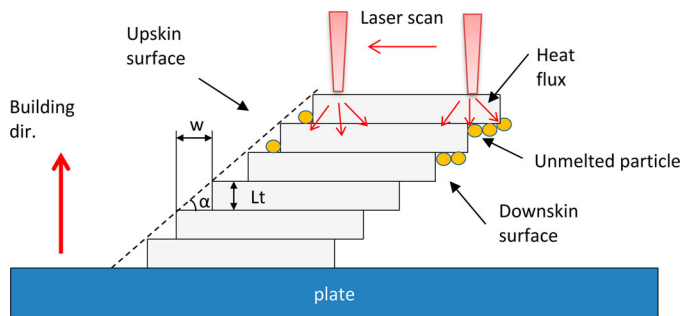


Figure 1. Schematic illustration of the ‘staircase effect’ in additive manufacturing [10,13,14].

Strano et al. [10] modeled arithmetic average height, R_a , on the inclined surface with the step angle, α , as in Equation (1)

$$R_a = \frac{1}{4} L_t \cos \alpha \quad (1)$$

where L_t represents the layer thickness.

In Equation (1), with a step angle of $\alpha = 90^\circ$, the theoretical arithmetic average height is 0. However, the experimentally measured arithmetic average height shows high R_a values due to un-melted powder particles stuck on the edges on the additively manufactured surfaces [15–17]. More un-melted particles were visible on the downskin surface than upskin one in the inclined additively manufactured surfaces [18,19], due to the difference in heat dissipation in upskin and downskin surfaces as shown in Figure 1. In the upskin surface, heat flux can flow into the previously constructed layer. On the other hand, in the downskin surface, laser irradiates directly the overhanging part and heat dissipation is lower, due to the low powder bed thermal conductivity. Thus, more un-melted particles can be stuck to the wall edges. Therefore, due to the layer-by-layer building in AM manufacturing, combined with powder sticking, high surface roughness on the LBM surface is always present ($R_a > 5\text{--}6\text{ }\mu\text{m}$) in spite of its high geometric freedom.

To reduce the high surface roughness of the AM surfaces, various post-processes, such as laser polishing [20], electro polishing [21], chemical polishing [22], and ultrasonic cavitation abrasive finishing [23], hydrodynamic cavitation abrasive finishing (HCAF) [24], have been tested. However, those post-processes are limited to open surfaces. On the other hand, abrasive flow machining (AFM) was recently shown to be effective to reduce the R_a value of the internal channel surfaces [25–32]. A schematic illustration of the AFM process is given in Figure 2.

As shown in Figure 2, the AFM medium, which is mixed with a polymeric carrier and abrasives, is filled in the lower cylinder. The upper cylinder is clamped, fixing the workpiece. The lower piston moves upward, making the AFM medium flow through the internal channel of the workpiece. The high pressure is applied to the flowing abrasives, removing

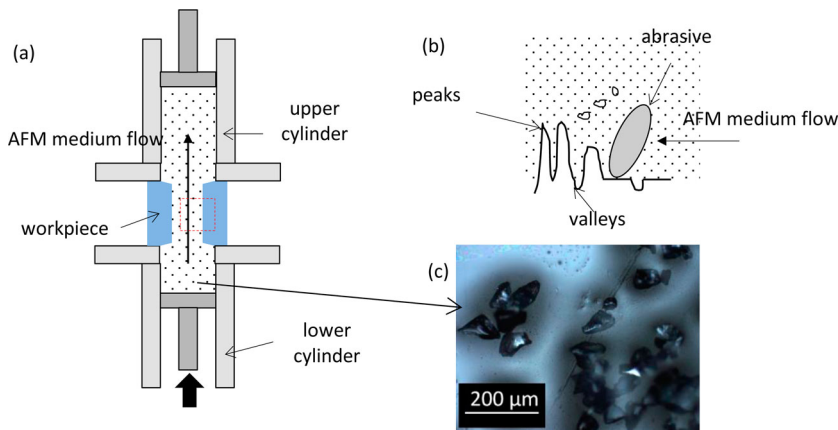


Figure 2. Schematic illustration of the AFM process: (a) two-way AFM machine, (b) material removal by the abrasive in the flowing AFM medium, and (c) abrasives (silicon carbide, SiC).

peak regions on the channel surface and improving its surface roughness. Han et al. [31] treated a long LBM-built internal channel ($\varnothing 3$ mm and 110-mm long) by AFM. They found a significant reduction in its surface roughness from 5.6 to 0.2 $\mu\text{m Ra}$.

The main objective of this study is to evaluate electromagnetic performances of laser beam melting (LBM) as-built and polished internal waveguides surfaces. Thus, four different types of waveguides were produced by LBM. To the author's knowledge, no attempt has been made to reduce surface roughness in internal surfaces of additive manufactured waveguides with the AFM process. The electromagnetic performance of as-built waveguides was compared with those of AFM finished internal surfaces.

2. Materials and methods

2.1. Design of waveguides

Four different types of waveguides were designed in this study. They are denoted as 'HR', 'WR42', 'GB', and 'TX1' as shown in Figure 3. All four waveguides have a rectangular cross section at two exits. However, in the middle of waveguides, two different cross-sectional shapes (e.g. rectangular and pentagonal) were used. As shown in Figure 3(b,d), the WR42 and TX1 waveguides have a rectangular cross-section, which is widely used in the waveguides in the literature. Considering manufacturing cost and electromagnetic performances, a dedicated 'Design for Additive Manufacturing Methodologies (DfAM)' methodology and an optimized cross-sectional shape for the waveguide were proposed in previous work [14,33]. As shown in Figure 3(a,c), the cross-section at the middle of HR and GB waveguides are pentagonal in shape. The wall thickness of all four types of waveguides is 1.5 mm.

2.2. Materials and manufacturing

Two different materials a titanium alloy (Ti6Al4V) and an aluminum alloy (AlSi7Mg0.6) were selected for the LBM process in this study. Titanium alloy (Ti6Al4V) has a low thermal diffusivity and aluminum alloy (AlSi7Mg0.6) exhibits good electrical conductivity. The powder compositions are presented in Table 1. The grain size distribution of the powder ranges from 10 to 90 μm for Ti6Al4V and from 25 to 65 μm for AlSi7Mg0.6.

All four types of waveguides were manufactured by the LBM process. The HR, WR42, and TX1 waveguides were manufactured with the PRO X300 SN machine (3D Systems). A process parameter optimization also was conducted on the SLM 125 HL machine (SLM solutions) to minimize surface roughness on the internal GB waveguide surface. The detailed parameter values are presented in Table 2. The layer height of waveguides ranges from 30 (for GB waveguide) to 50 μm (for HR, WR42, and TX1 waveguides). The WR42 and TX1 waveguides with a rectangular cross-section were manufactured at 45° toward the plate as shown in Figure 3(b,d). On the other hand, as shown in Figure 3(a,c), the HR and GB waveguides with a pentagonal cross-section were built parallel to the plate.

An LBM-produced HR waveguide is shown in Figure 4. After the LBM process, all the parts were post-treated. The remaining powders were removed from the waveguides. A residual stress relief was carried out with a 2 h – 300°C heat treatment. External support structures were removed by machining. Two flanges of the waveguide were also machined to remove support structures.

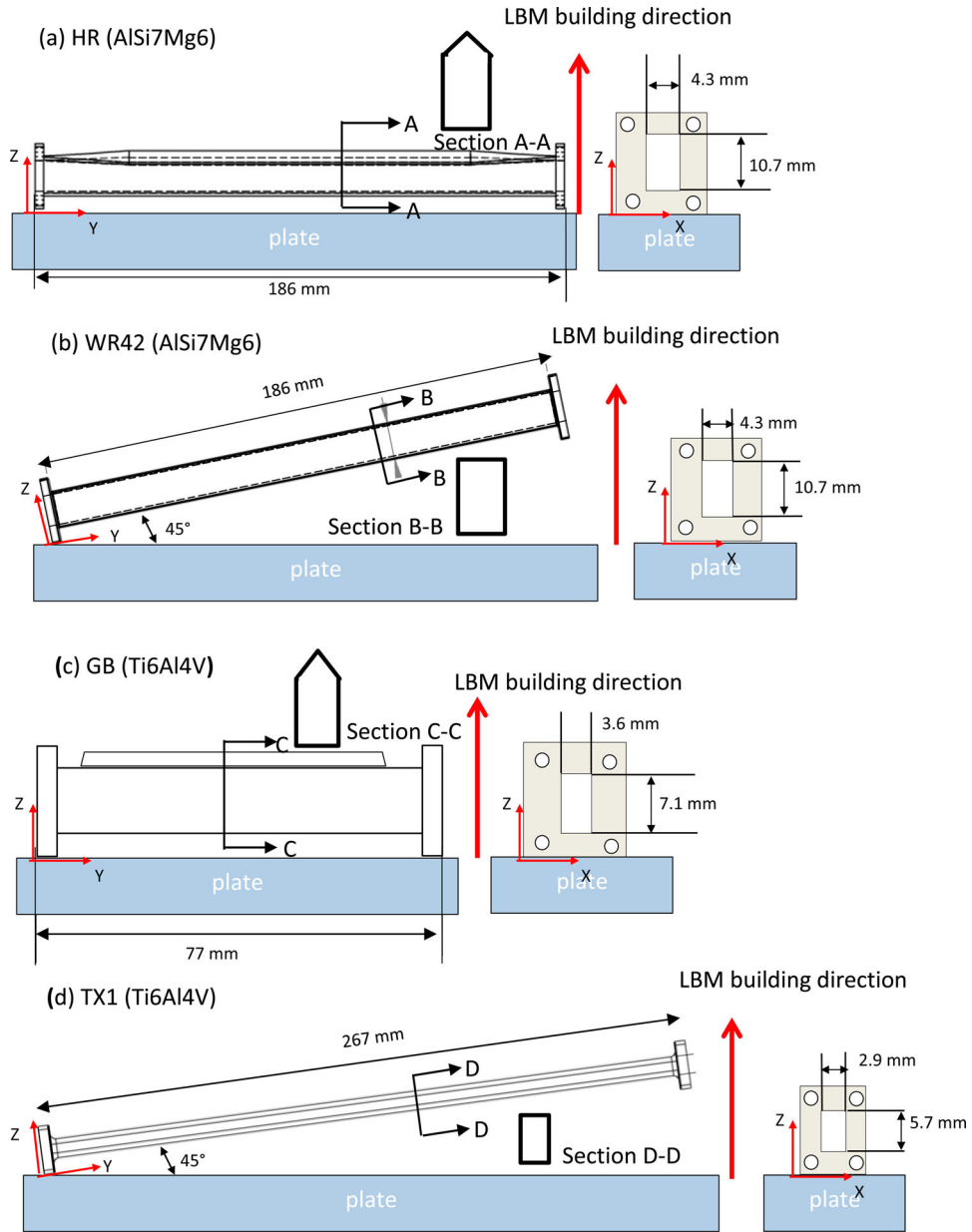


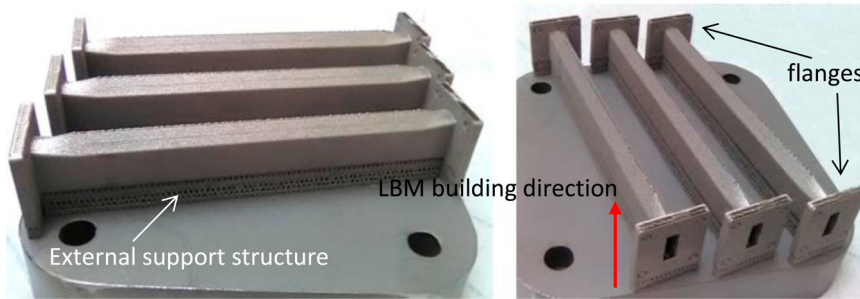
Figure 3. Shapes and dimensions of the four types of waveguides: (a) HR (AlSi7Mg0.6), (b) WR42 (AlSi7Mg0.6), (c) GB (Ti6Al4V), and (d) TX1 (Ti6Al4V). (All waveguides have two rectangular exits. Cross-sectional shapes at the middle of waveguides are also indicated.)

Table 1. Chemical composition of Ti6Al4V and AlSi7Mg0.6 powders (in %).

Ti6Al4V								
Al	V	C	O	N	Fe	H	Other	Ti
5.5–6.5	3.5–4.5	0.08	0.13	0.03	0.25	0.0125	0.1	Remainder
AlSi7Mg0.6								
Fe	Si	Mn	Zn	Ti	Mg	Cu	O	Al
< 0.19	6.5–7.5	< 0.10	< 0.07	< 0.25	0.45–0.70	< 0.05	< 0.1	Remainder

Table 2. LBM process parameters used to build waveguides.

Surface	Laser power (W)	Scanning speed (mm/s)	Hatch (μm)
Contour	150	450	–
Core	225	1100	120
Downskin	100	1100	60
Upskin	100	100	80

**Figure 4.** LBM-produced HR waveguide (AlSi7Mg0.6).

2.3. AFM treatment

The AFM surface treatment was performed in the two-way AFM machine (VECTOR 200, Extrude Hone[®]). An experimental setup for AFM of internal surfaces of the HR (AlSi7Mg0.6) waveguide is shown in Figure 5.

The AFM process parameters, such as volume of AFM medium per one cycle (V_{cylinder}), AFM pressure (P), number of cycles (N), and related measured and calculated values [32], such as cross-section area of the channel (A), one cycle time (t_{cycle}) and the velocity of AFM flow (v_1) are listed in Table 3.

As shown in Figure 5, the AFM medium flows through the internal channel of the HR waveguide. Some additional fixture parts were used to perform AFM of internal surfaces of the HR waveguide. The sleeve was used to resist the clamping pressure of the two cylinders of the AFM machine. Thus, the clamping pressure is not applied to the waveguide itself. The support part was designed to avoid a possible buckling or deformation of the waveguide because the HR waveguide has a thin wall thickness of $t = 1.5$ mm. Two covers, which connect the internal channel of the waveguide to two cylinders, have a tapered geometry. Thus, the high pressure of the AFM medium can be applied to the internal channel surface of the waveguide during AFM. In this process, the AFM medium (ULV50%-54, Extrude Hone[®]) composed of silicon carbide abrasives (SiC) with 50 wt.% and polymer carrier

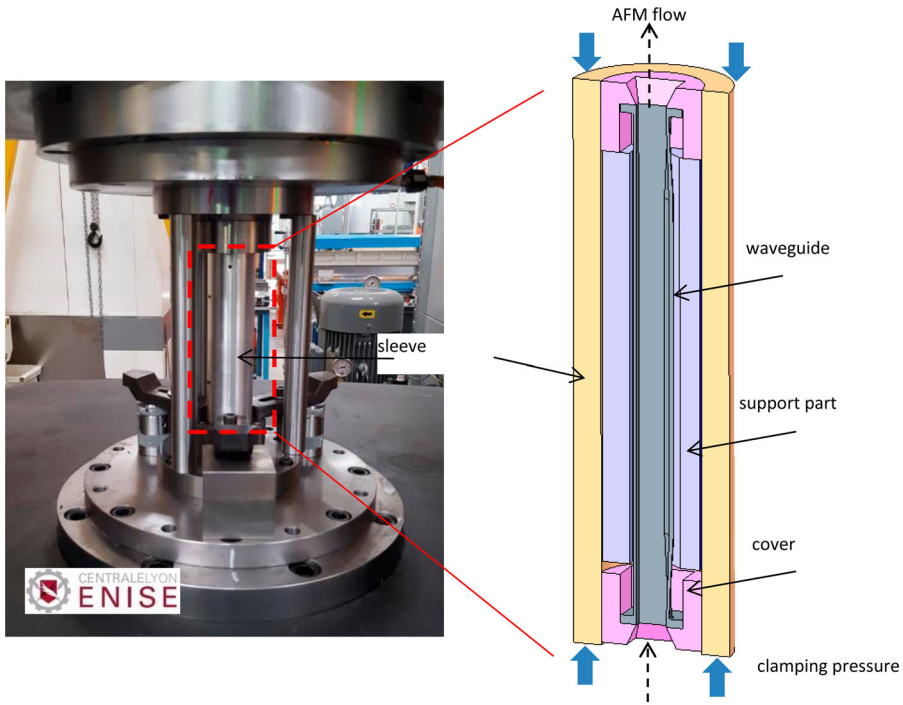


Figure 5. Experimental setup for AFM of internal surfaces in the HR (AlSi7Mg0.6) waveguide and its cross-section view equipped in the fixture parts.

Table 3. Process parameters and related values for the AFM finish.

	Volume of AFM medium per one cycle, V_{cylinder} (mm ³)	AFM pressure, P (bars)	Number of cycles, N	Cross-section area of the channel, A (mm ²)	One cycle time, t_{cycle} (sec)	Velocity of AFM flow, v_1 (mm/sec)
HR (AlSi7Mg0.6)	655,482.56	70	12	46.4	90	157
WR42(AlSi7Mg0.6)	655,482.56	40	5	46.4	90	157
GB (Ti6Al4V)	655,482.56	70	30	16.2	47	553
TX1 (Ti6Al4V)	327,741.28	70	25	25.2	132	153

(polyboroxane) was employed. It has ultra-low viscosity of 200 Pa s and grain size of 54 grit (about 350 μm).

In the previous study [32], the velocity of AFM flow, v_1 , can be calculated using Equation (2)

$$v_1 = \frac{V_{\text{cylinder}}}{t_{\text{cycle}} \times A} \quad (2)$$

2.4. Measurements of surface roughness of internal surfaces

To verify the progress of the surface roughness of internal surfaces in the waveguides, its surface roughness before and after AFM was measured. A profilometer (Talysurf 50, Talyor Hobson) was used to measure their surface roughness. It can be noted that the cross-section areas of channels of waveguides are relatively small as shown in Figure 3. Thus, a small

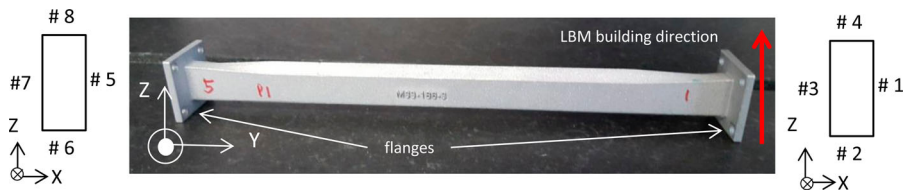


Figure 6. Numbering of the internal surfaces in the waveguide.

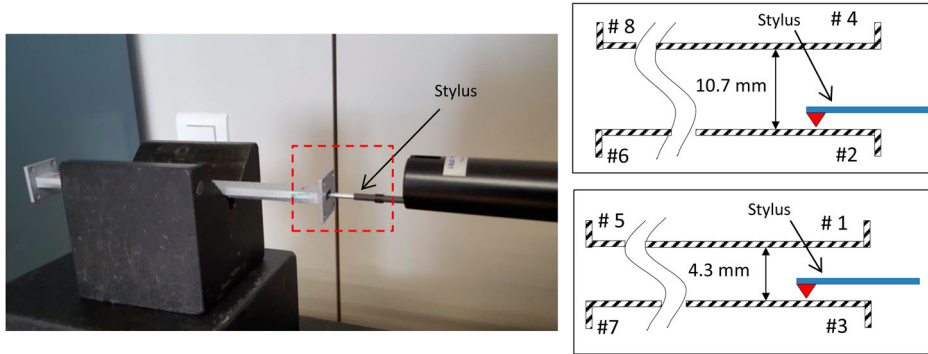


Figure 7. Measurement of the surface roughness of the internal channel (the HR waveguide) and its cross-section view to measure internal surfaces #2 and #3.

stylus (112/2623, Talyor Hobson) to fit into the rectangular channel was adopted. Its stylus tip radius is $2\text{ }\mu\text{m}$. The waveguide has two exits with flanges. Their cross-sections in the exit regions are rectangular in shape. Each surface was numbered from #1 to #8 in Figure 6. The measurement of the internal channels surface roughness is shown in Figure 7. Townsend et al. [34] stated that, in the measurement of surface roughness of the additive manufactured surface, a cut-off filter and scanning length can be selected depending on its surface geometry and area. In this study, the LBM produced internal channels are very narrow and have small surface areas. Thus, a cut-off filter of $L_c = 0.8\text{ mm}$ and a scanning length of $l = 4\text{ mm}$ were used to obtain surface roughness parameters.

2.5. Measurements of the S-parameters

The S-parameters were measured using a vector network analyzer (VNA). The model used in this study has the following characteristics (Table 4).

The measurements were made at room temperature ($20\text{--}26\text{ }^{\circ}\text{C}$). The instrument reached thermal equilibrium after turning it on for 1 h. The device was calibrated with a power of 0 dB, at a band of 1 kHz bandwidth with 272 measurement points.

3. Results

3.1. Surface topographies of waveguide's internal surface before and after AFM

Figure 8 shows surface topographies of the internal surface #8 of the aluminium waveguide, WR42 (AlSi7Mg0.6). The X- and Y-axis in Figure 8 corresponds to those in Figure 3(b).

Table 4. Characteristics of the vector network analyzer (VNA).

Model	Rhode & Schwarz – ZVK
Manufacturer reference	10–40 MHz
Frequency resolution	100 μ Hz
Impedance	50 Ω
Measuring time	< 0.7 ms/point
Bandwidth	18–22 / 33–46 GHz
Measurement error – Reflection	2 dB
Measurement error – Transmission	0.2 dB
Number of points	406

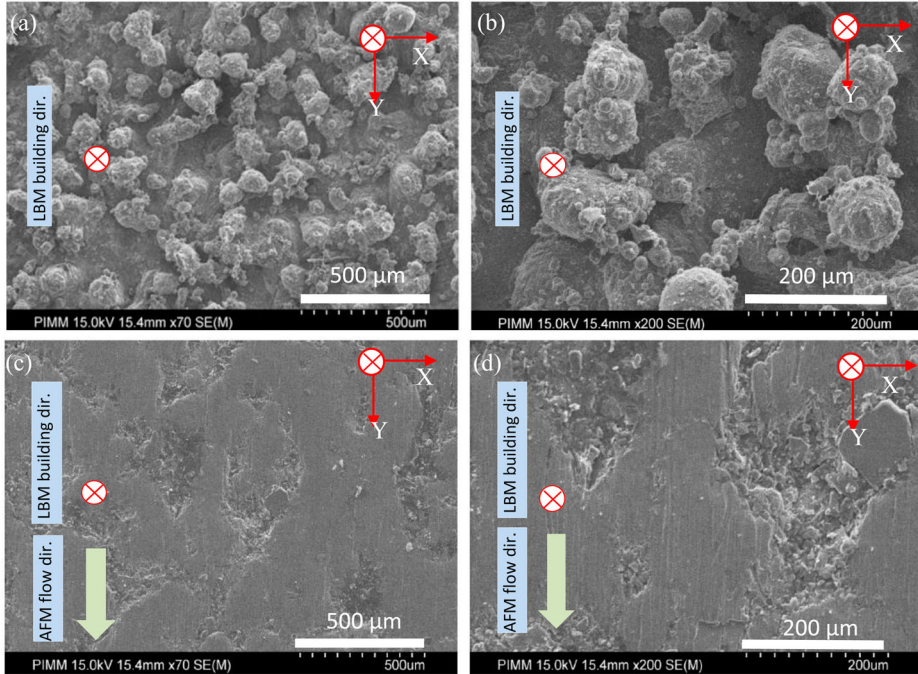


Figure 8. SEM micrographs of the internal surface #8 of the waveguide, WR42 (AlSi7Mg0.6): (a, b) LBM as-built and (c, d) AFM finished surfaces.

As shown in Figure 8(a,b), un-melted powders are visible on the LBM as-built surface. The LBM building direction corresponds to the Z-axis. After the AFM process, these un-melted powders from additive manufacturing were shown to be removed as shown in Figure 8(c). The AFM flow direction is indicated with an arrow. Its surface is characterized by AFM flow marks, caused by micro-abrasion between abrasives and the internal surface.

The AFM surface topography was observed at higher magnification in Figure 8(d). It shows that most of the high peak regions of the initial LBM surface were removed whereas valley regions still remained. A similar trend of the surface topography is observed in the surface profile measured with a profilometer in Figure 9.

Roughness parameters of LBM and AFM finished surfaces are compared, considering surface #3 of the WR42 (AlSi7Mg0.6) waveguide to understand material removal and surface roughness improvement (Table 5). After 5 cycles of AFM, a significant reduction of the

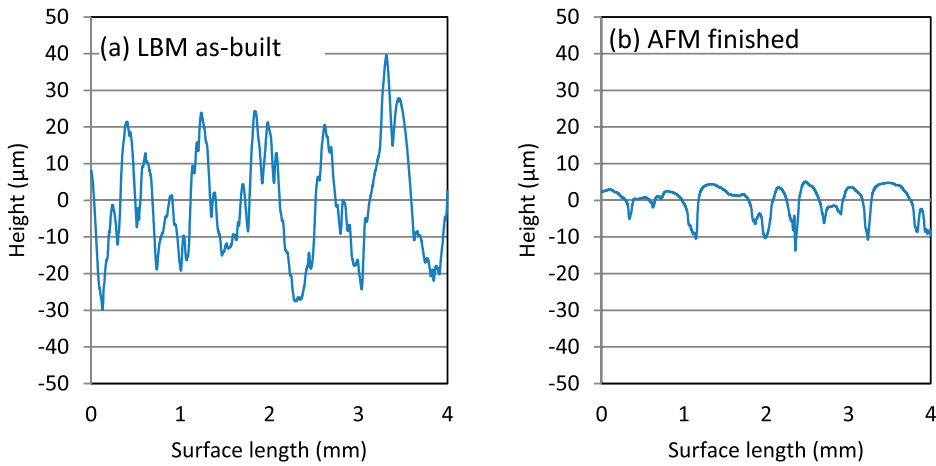


Figure 9. Surface profile of the internal surface of WR42 (AlSi7Mg0.6) waveguide: (a) LBM as-built and (b) AFM finished surfaces.

Table 5. Surface roughness parameters in LBM as-built and AFM finished internal surface of WR42 (AlSi7Mg0.6) waveguide.

Surface roughness parameters		LBM as-built	AFM finished (after 5 cycles)
Arithmetic average height (μm)	Ra	11.9	3.1
Root mean square height of the surface (μm)	Rq	14.2	4.0
Maximum height (μm)	Rz	54.8	16.6
Reduced peak height (μm)	Rpk	23.2	0.1

arithmetic average roughness from 11.9 to 3.1 μm Ra was observed. As discussed in their surface topography comparison in Figure 8, most of the peak regions in the LBM surface were removed, leaving AFM flow marks after AFM. This observation agrees with a significant reduction in a reduced peak height from 23.2 to 0.1 μm Rpk after AFM. Arithmetic average heights, Ra , of internal surfaces for the four types of waveguides before and after AFM are shown in Figure 10. The corresponding material and the numbering of surfaces in two exit regions (see Figure 6) of each waveguide are also indicated. It can be noted that variations of Ra values in the different as-built surfaces (before AFM) in Figure 10 are commonly observed in the additively manufactured surfaces built at different angles, such as top, down, side skins [33].

After AFM finishing for 12 cycles of the HR internal channel, its average Ra value was lowered to 0.7 μm Ra . A significant improvement from 12.2 to 3.9 μm Ra was also seen in the WR42 internal channels after only 5 AFM cycles. Both HR and WR42 waveguides were fabricated using aluminum alloy (AlSi7Mg6) powder. On the other hand, much higher cycles were logically required to reduce Ra values on internal surfaces in the GB and TX1 waveguides built with titanium alloy (Ti6Al4V) powder, because titanium is a difficult-to-machine material. Especially, TX1 has the smallest cross-section area (5.7 mm \times 2.9 mm) and the longest channel length (267 mm) among waveguides in this study, yielding the longest one cycle time, t_{cycle} , and the lowest velocity of AFM flow, v_1 (see Table 3). Thus, the progress of Ra value was the lowest even after AFM for 25 cycles. Average Ra values of internal surfaces of four waveguides before and after AFM are shown in Figure 11.

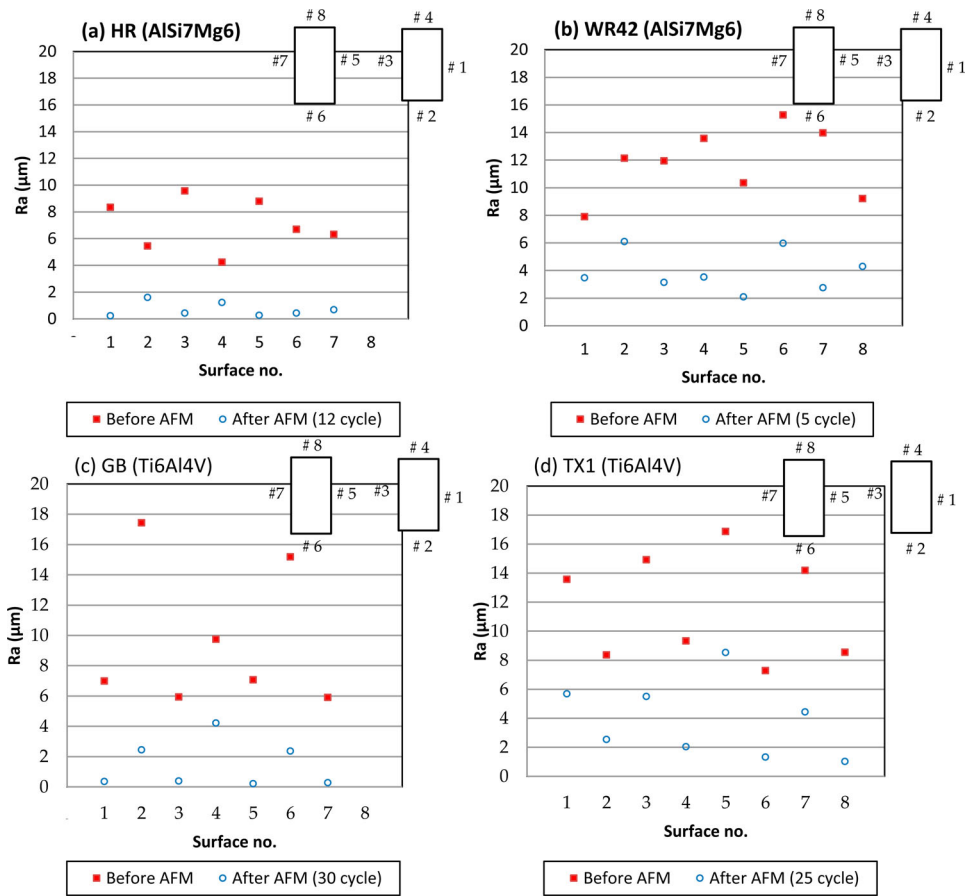


Figure 10. Arithmetic average roughness (R_a value) in internal surfaces in two exit regions of all types of waveguides before and after AFM: (a) HR(AlSi7Mg0.6), (b) WR42(AlSi7Mg0.6), (c) GB (Ti6Al4 V), and (d) TX1 (Ti6Al4 V). (R_a values in the surface #8 in (a) HR and (b) WR42 were not presented because their initial R_a values were affected by remaining support materials.)

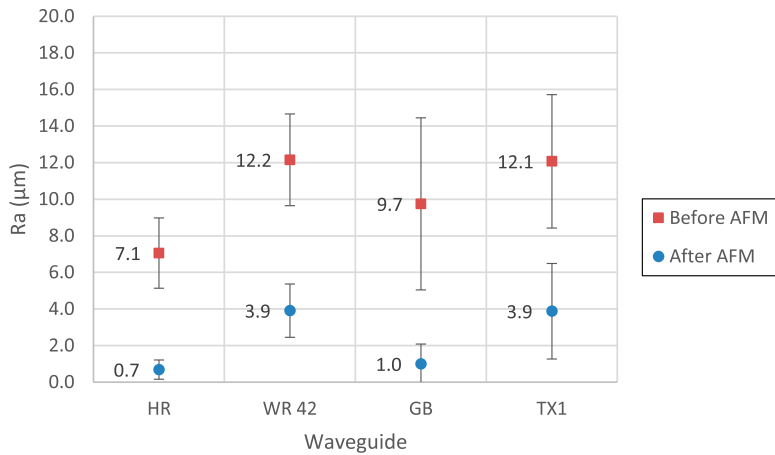


Figure 11. Average R_a values of internal surfaces of four waveguides before and after AFM.

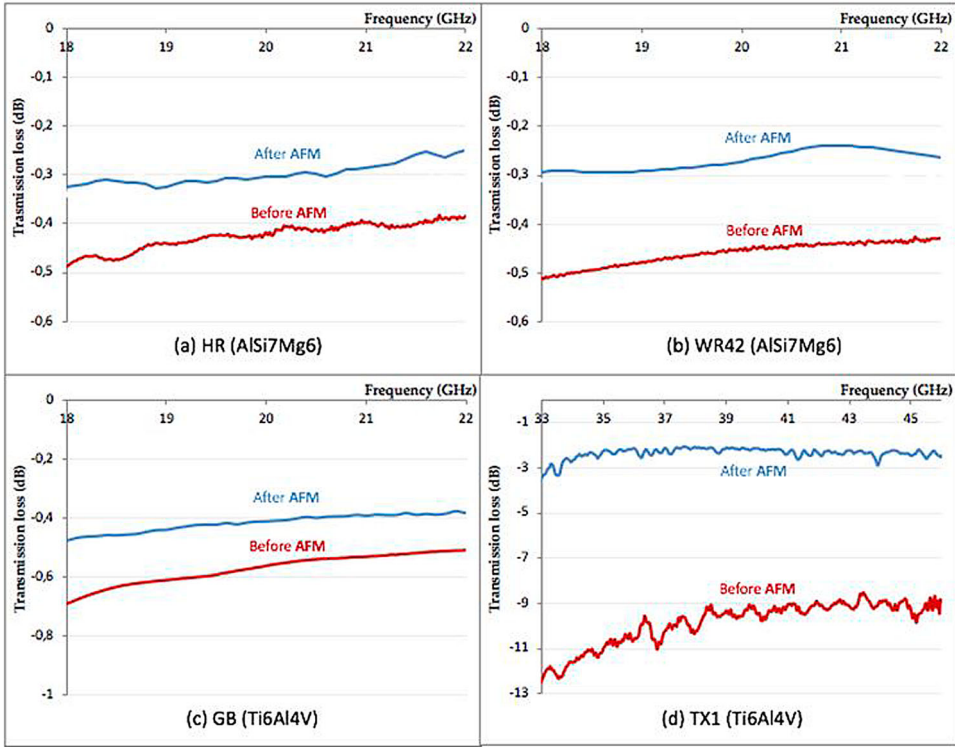


Figure 12. Transmission loss in all four types of waveguides with LBM as-built (before AFM) and AFM finished (after AFM) internal channels: (a) HR (AlSi7Mg0.6), (b) WR42 (AlSi7Mg0.6), (c) GB (Ti6Al4 V), and (d) TX1 (Ti6Al4 V).

In summary, a significant reduction in Ra values of internal surfaces in all four waveguides was observed after AFM. Thus, the electromagnetic performances of LBM as-built and AFM finished waveguides are measured and compared in the next section.

3.2. Electromagnetic performances of LBM as-built and AFM finished waveguides

Electromagnetic performances of the four LBM as-built and AFM finished waveguides are compared in Figure 12. The transmission loss of aluminum HR and WR42 waveguides was measured over the bandwidth (18–22 GHz). A significant reduction of transmission loss was observed in AFM finished waveguides as compared to as-built LBM ones.

As shown in Figure 12(a,b), the power loss through the 186-mm-long as-built waveguides was approximately 10% as compared to the input power (−0.5 dB vs. −0.4 dB at 18 GHz). On the other hand, with waveguides having AFM finished internal surface, the power loss was estimated to be about 6% (−0.3 dB vs. −0.25 dB at 18 GHz), showing a significant reduction in the power loss.

In Figure 12(c), the power loss at 18 GHz in the LBM as-built titanium GB waveguides seems to be much higher than that in the aluminum LBM as-built HR waveguides (−0.7 dB vs. −0.5 dB), although the titanium alloy GB waveguide is shorter than aluminium alloy HR ones (77 vs. 186 mm). The higher electrical conductivity of aluminum alloy (AlSi7Mg6)

Table 6. Average Ra values and power losses in four types of waveguides with LBM as-built and AFM finished internal surfaces.

Waveguide	LBM as-built surface		AFM finished surface	
	Average Ra (μm)	Average power loss (dB)	Average Ra (μm)	Average power loss (dB)
HR (AlSi7Mg0.6)	7.1	−0.44	0.7	−0.28
WR42 (AlSi7Mg0.6)	12.2	−0.45	3.9	−0.27
GB (Ti6Al4 V)	9.7	−0.58	1.0	−0.40
TX1 (Ti6Al4 V)	12.1	−10.3	3.9	−2.2

compared to that of titanium alloy (Ti6Al4V) can explain such a smaller power loss. After AFM machining, the power loss of the GB waveguide ranges from −0.47 to −0.38 dB, showing a significant reduction.

In Figure 12(d), the power loss in titanium TX1 waveguides was measured between 33 and 46 GHz. The power loss in the LBM as-built TX1 waveguide ranges from −12 to −9 dB while the AFM finished waveguides exhibit a substantial reduction, with power loss values between −3 and −2.3 dB. Average Ra values and power losses in four waveguides with LBM as-built and AFM finished internal surfaces are summarized in Table 6.

In all four waveguides, a reduction in power loss was seen in the AFM finished internal surfaces as compared to LBM as-built ones. Similar trends were observed in other post-processed additively manufactured surfaces. Tchhoffolo-Talom and Turpault [2] found about 0.2 dB reduction in transmission loss in the band (26–34 GHz) in the Surtec 650 chemical treated aluminium (AS10G) waveguide surface. They also found about 2 dB reduction in transmission loss in the band (26–34 GHz) in the silver-plated titanium (Ti6Al4V) waveguide surface. Martin-Guennou et al. [35] observed that transmission loss decreased about 0.2 dB in the K band (12–40 GHz) and Q band (33–50 GHz) in the gold or silver-plated aluminium (AlSi10Mg) waveguide surfaces.

4. Discussion

The attenuation of electromagnetic fields in a real conductor due to the propagation of electrons in the skin thickness (a few microns) causes power loss during the propagation of the fundamental mode TE₁₀. The attenuation constant, $\alpha_{c,TE10}$, for the fundamental mode TE₁₀ [36] can be expressed as

$$\alpha_{c,TE10} = 8668 \frac{\sqrt{(\pi \mu f / \sigma)}}{b \sqrt{\mu / \varepsilon}} \frac{1 + (2b/a)(f_c/f)^2}{\sqrt{1 - (f_c/f)^2}} \quad (3)$$

where μ is the magnetic permeability of the material and f is the frequency of use. f_c is the cutoff frequency. σ represents the electrical conductivity of the material. a and b are the cross-section dimensions of the waveguide. ε is the dielectric permittivity of the material.

In Equation (3), higher electrical conductivity can lead to lower attenuation constant, $\alpha_{c,TE10}$, reducing transmission loss. Surface roughness affects electrical conductivity of the material. Thus, effective electrical conductivity, $\sigma_{\text{effective}}$, can be expressed as

$$\sigma_{\text{effective}} = K \sigma_{\text{theory}} \quad (4)$$

where K is a correction coefficient, which depends on the surface roughness of the conductive material. In Morgan et al. [37], the correction coefficient, K , can be defined

as

$$K = \left[1 + \frac{2}{\pi} \cdot \arctan \left[1.4 \left(\frac{Rq}{\delta} \right)^2 \right] \right] \quad (5)$$

where Rq is the root mean square height of the surface and δ is the skin thickness. Thus, with effective electrical conductivity, $\sigma_{\text{effective}}$, Equation (3) can be expressed as

$$\alpha_{c,TE10} = 8668 \frac{\sqrt{\pi f \varepsilon}}{b \sqrt{K \sigma_{\text{theory}}}} \frac{1 + (2b/a)(f_c/f)^2}{\sqrt{1 - (f_c/f)^2}} \quad (6)$$

In Equation (4), as surface roughness increases, the correction coefficient, K , becomes close to 0. Consequently, the attenuation constant, $\alpha_{c,TE10}$, increases in Equation (6). On the other hand, as surface roughness decreases, K reaches 1 in Equation (5). Thus, the attenuation constant decreases, suggesting that waveguides can transmit more input power. As a result, more electrical currents propagate through the internal surfaces.

Braunisch et al. [9] calculated an attenuation constant to account for propagation loss due to rough and smooth conductors. Martin-Guennou et al. [35] showed that in a very rough as-built additive manufactured surface with quadratic surface mean roughness of $RSq = 32 \mu\text{m}$, surface roughness significantly contributed to transmission loss in the K and Q bands. In this study, the average surface roughness of as-built LBM surfaces of four waveguides ranges from 7 to $12 \mu\text{m Ra}$. The average surface roughness of the AFM finished surfaces ranges from 0.7 to $3.9 \mu\text{m Ra}$. The surface roughness in the AFM finished waveguide's internal surfaces is an equivalent level of those in other post-processed surfaces, such as gold electroplated SLM Su-15Sn ($1.29 \mu\text{m Sa}$) or manually polished SLM Su-15Sn surfaces ($2.79 \mu\text{m Sa}$) in the study done by Zhang et al. [38]. As discussed in Section 3.2, reduction in transmission loss in the AFM finished surfaces showed similar trends as those in other studies. Thus, a high reduction in surface roughness by the AFM process can significantly contribute to a decrease in transmission loss in four waveguides in the K and Q bands in this study.

5. Conclusions

In this study, four waveguides (e.g. GB, WR42, GB, and TX1) in aluminium (AlSi7Mg6) and titanium (Ti6Al4V) alloys were designed and produced by the LBM process. Their internal surface exhibited high arithmetic average height (around $7\text{--}12 \mu\text{m Ra}$). Thus, their internal surfaces were finished by AFM, substantially reducing arithmetic average height down to $0.7\text{--}3.9 \mu\text{m Ra}$. Electromagnetic performances of all four waveguides were evaluated in terms of power loss. The results showed that a significant reduction in power loss for AFM finished waveguides compared to LBM as-built ones. This confirms the ability of LBM technologies combined with AFM post-processing to design and manufacture waveguides with high geometric freedom and adequate electromagnetic performances.

Acknowledgements

The 'La région Auvergne Rhône-Alpes' in France is acknowledged for funding the purchase of the AFM machine (Extrude Hone[®]). A special thank goes to Extrude Hone for providing the AFM

medium. The authors are grateful to M. Cici, H. Seux, and P. Polly for making and modifying the fixture parts.

Disclosure statement

No potential conflict of interest was reported by the author(s).

Funding

This work was supported by I@L Carnot MELTED.

Notes on contributors

Mathieu François received his MSc in Mechanics, Materials and Processes from Arts et Métiers ParisTech School of Engineering in 2016. He received his PhD from Arts et Métiers ParisTech, Paris, France, in 2020. He worked as a PhD candidate at Thales SIX GTS France with a partnership with Arts et Métiers ParisTech School of Engineering and the French National Center for Scientific Research.

Sangil Han is a Postdoctoral Researcher of Laboratoire de Tribologie et Dynamique des Systèmes (LTDS) at the Université de Lyon, Ecole Centrale de Lyon – ENISE, France. He received his BS in agricultural machinery and process engineering from Seoul National University, South Korea, in 2000, and his PhD in mechanical engineering from the Georgia Institute of Technology, GA, USA, in 2006. He previously worked as a Senior Research Engineer at Samsung Electronics, South Korea. His research interest aims at experiment and modeling hard turning, abrasive flow machining (AFM) and sequence machining.

Frédéric Segonds is an Associate Professor of Mechanical Engineering at Arts et Métiers ParisTech, Paris, France and a member of the Product Design and Innovation Laboratory (LCPI). His research interest aims at ‘Creativity and Design With/For/By Additive Manufacturing’.

Corinne Dupuy is a Researcher of the Processes and Engineering in Mechanics and Materials Laboratory (PIMM), Paris, France.

Mickaël Rivette is an Associate Professor of Arts et Métiers ParisTech, Metz, France and a member of the Manufacturing Engineering and Control Laboratory (LCFC). His research interest focuses on design for additive manufacturing.

Simon Turpault is an Engineering Technologist of Thales SIX GTS France, Cholet, France. He is specialized in materials, processes, and additive manufacturing.

Mehdi Mimouna is a Researcher of OPS-Hardware Techno. Tools & Engineering, Thales SIX GTS France, Gennevilliers, France

Ferdinando Salvatore is an Associate Professor of Laboratoire de Tribologie et Dynamique des Systèmes (LTDS) at the Université de Lyon, Ecole Centrale de Lyon – ENISE, France. His research focuses on finishing processes, such as abrasive flow machining (AFM), drag finishing, and electrochemical mechanical polishing.

Joël Rech is a Professor of Laboratoire de Tribologie et Dynamique des Systèmes (LTDS) at the Université de Lyon, Ecole Centrale de Lyon – ENISE, France. He leads a research group of 23 people working on the characterization and modelling of physical phenomena at the tool/work material interface in cutting and superfinishing operations. He made remarkable breakthroughs in numerical modeling of surface integrity induced by cutting and polishing processes (residual stresses, roughness, microstructure) and in modeling of tribological phenomena (friction, wear etc.) of cutting tools.

Patrice Peyre is a Research Director of Arts et Métiers ParisTech, Paris, France and a member of the Processes and Engineering in Mechanics and Materials Laboratory (PIMM) and the French National Center for Scientific Research. His research focuses on material science, laser processes and additive manufacturing.

ORCID

Mathieu François  <http://orcid.org/0000-0002-2133-1605>

Frédéric Segonds  <http://orcid.org/0000-0001-5677-4257>

Mickaël Rivette  <http://orcid.org/0000-0001-5840-1307>

Patrice Peyre  <http://orcid.org/0000-0002-3679-9622>

References

- [1] Kilian M, Hartwanger C, Schneider M, et al. Waveguide components for space applications manufactured by additive manufacturing technology. *IET Microw. Antennas Propag.* **2017**;11:1949–1954.
- [2] Tchhoffolo-Talom F, Turpault S. Additive manufacturing for rf microwave devices: design, performances and treatments improvement evaluations. 2017 International Conference on electromagnetics in advanced applications (ICEAA); **2017**; p. 1473–1476.
- [3] Zhang B, Guo Y-X, Zirath H. Investigation on 3d-printing technologies for millimeter-wave and terahertz applications. *Proc IEEE.* **2017**;105:723–736.
- [4] Booth P, Lluch EV. Enhancing the performance of waveguide filters using additive manufacturing. *Proc IEEE.* **2017**;105:613–619.
- [5] Lorente JA, Mendoza MM, Petersson AZ, et al. Single part microwave filters made from selective laser melting. 2009 European microwave conference (EuMC); **2009**. p. 1421–1424.
- [6] Zhang B, Zirath H. 3D printed iris bandpass filters for millimetre-wave applications. *Electron Lett.* **2015**;51(22):1791–1793.
- [7] Guo C, Shang X, Lancaster MJ, et al. A 3-d printed lightweight x-band waveguide filter based on spherical resonators. *IEEE Microw Wirel Compon Lett.* **2015**;25(7):442–444.
- [8] Wang R, Cui W. A rapid estimation of the conductor loss in the rectangular waveguide with rough surface. 2011 4th IEEE International symposium on microwave, antenna, propagation and EMC technologies for wireless communications; **2011**. p. 11.
- [9] Braunisch H, Gu X, Camacho-Bragado A, et al. Off-chip rough-metal surface propagation loss modeling and correlation with measurements. 2007 Proceedings 57th Electronic components and technology conference; **2007**. p. 785–791.
- [10] Strano G, Hao L, Everson RM, et al. Surface roughness analysis, modelling and prediction in selective laser melting. *J Mater Process Technol.* **2013**;213(4):589–597.
- [11] Campbell RI, Martorelli M, Lee HS. Surface roughness visualisation for rapid prototyping models. *Comput.-Aided Des.* **2002**;34:717–725.
- [12] Yadroitsev I, Smurov I. Surface morphology in selective laser melting of metal powders. *Phys Procedia.* **2011**;12:264–270.
- [13] Cabanettes F, Joubert A, Chardon G, et al. Topography of as built surfaces generated in metal additive manufacturing: a multi scale analysis from form to roughness. *Precis Eng.* **2018**;52:249–265.
- [14] François M. Conception pour la fabrication additive, par fusion laser sur lit de poudre, de composants hyperfréquences (in French) [Ph.D. thesis], École Nationale Supérieure d'Arts et Métiers; **2020**
- [15] Triantaphyllou A, Giusca AL, Macaulay GD, et al. Surface texture measurement for additive manufacturing. *Surf Topogr: Metrol Prop.* **2015**;3(2):024002.
- [16] Fox JC, Moylan SP, Lane B. Effect of process parameters on the surface roughness of overhanging structures in laser powder bed fusion additive manufacturing. *Procedia CIRP 2016 3rd CIRP Conf. Surf. Integr.* **2016**;45:131–134.

- [17] Hartunian P, Eshraghi M. Effect of build orientation on the microstructure and mechanical properties of selective laser-melted Ti-6Al-4V alloy. *J Manuf Mater Process*. 2018;2(69):1–13.
- [18] Lerebours A, Vigneron P, Bouvier S, et al. Additive manufacturing process creates local surface roughness modifications leading to variation in cell adhesion on multifaceted Ti6Al4 V samples. *Bioprinting*. 2019;16:e00054.
- [19] Koutiri I, Pessard E, Peyre P, et al. Influence of SLM process parameters on the surface finish, porosity rate and fatigue behavior of as built inconel 625 parts. *J Mater Process Technol*. 2018;255:536–546.
- [20] Marimuth S, Triantaphyllou A, Antar M, et al. Laser polishing of selective laser melted components. *Int J Mach Tool Manu*. 2015;95:97–104.
- [21] Urlea V, Brailovski V. Electropolishing and electropolishing-related allowances for powder bed selectively laser-melted Ti-6Al-4V alloy components. *J Mater Process Technol*. 2017;242:1–11.
- [22] Lyczkowska E, Szymczyk P, Dybala B, et al. Chemical polishing of scaffolds made of Ti-6Al-7Nb alloy by additive manufacturing. *Arch Civ Mech Eng*. 2014;14:586–594.
- [23] Yeo KL, Tan KL. Surface modification of additive manufactured components by ultrasonic cavitation abrasive finishing. *Wear*. 2017;378-379:90–95.
- [24] Nagalingam AP, Yuvaraj HK, Santhanam V, et al. Multiphase hydrodynamic flow finishing for surface integrity enhancement of additive manufactured internal channels. *J Mater Process Tech*. 2020;283(116692):1–21.
- [25] Jain VK, Adsul SG. Experimental investigations into abrasive flow machining (AFM). *Int J Mach Tool Manu*. 2000;40:1003–1021.
- [26] Kumar S, Hiremath SS. A review on abrasive flow machining (AFM). *Proc Technol*. 2016;25:1297–1304.
- [27] Uhlmann E, Mihotovic V, Roßkamp S, et al. A pragmatic modeling approach in abrasive flow machining for complex-shaped automotive components. *Procedia CIRP*. 2016;46:51–54.
- [28] Duval-Chaneac MS, Han S, Claudin C, et al. Experimental study on finishing of internal laser melting (SLM) surface with abrasive flow machining (AFM). *Precis Eng*. 2018;54:1–6.
- [29] Duval-Chaneac MS, Han S, Claudin C, et al. Characterization of maraging steel 300 internal surface created by selective laser melting (SLM) after abrasive flow machining (AFM). *Procedia CIRP*. 2018;77:359–362.
- [30] Han S, Salvatore F, Rech J. Residual stress profiles induced by abrasive flow machining (AFM) in 15-5PH stainless steel internal channel surfaces. *J Mater Process Technol*. 2019;267:348–358.
- [31] Han S, Salvatore F, Rech J, et al. Surface integrity in abrasive flow machining (AFM) of internal channels created by selective laser melting (SLM) in different building directions. *Procedia CIRP 5th CSI*. 2020;87:315–320.
- [32] Han S, Salvatore F, Rech J, et al. Abrasive flow machining (AFM) finishing of conformal cooling channels created by selective laser melting (SLM). *Precision Eng*. 2020;64:20–33.
- [33] François M, Segonds F, Rivette M, et al. Design for additive manufacturing methodologies (DfAM): a proposal to foster the design of microwave waveguide components. *Virtual Phys Prototyp*. 2019;14(2):175–187.
- [34] Townsend S, Senin N, Blunt L, et al. Surface texture metrology for metal additive manufacturing: a review. *Precision Eng*. 2016;46:34–47.
- [35] Martin-Guennou A, Quéré Y, Rius E, et al. Direct metal laser sintering process investigation: application to 3-D slotted waveguide antennas. *IET Microw Antennas Propag*. 2017;11:1921–1929.
- [36] Klinbun W, Rattanadecho P, Pakdee W. Microwave heating of saturated packed bed using a rectangular waveguide (TE10 mode): influence of particle size, sample dimension, frequency, and placement inside the guide. *Int J Heat Mass Transf*. 2011;54:1763–1774.
- [37] Morgan SP. Effect of surface roughness on eddy current losses at microwave frequencies. *J Appl Phys*. 1949;20:352–362.
- [38] Zhang B, Chen W, Wu Y, et al. Review of 3D printed millimeter-wave and tetrahertz passive devices. *Int J Antennas Propag*. 2017;6:1–10.